The Astrophysical Journal, 976:252 (9pp), 2024 December 1 https://doi.org/10.3847/1538-4357/ad86bf

Could the Recent Rebrightening of the GW170817A Afterglow Be Caused by a Counterjet?

Ranadeep G. Dastidar and Paul C. Duffell
Department of Physics and Astronomy, Purdue University, 525 Northwestern Avenue, West Lafayette, IN 47907, USA
Received 2024 May 31; revised 2024 September 27; accepted 2024 October 13; published 2024 November 27

Abstract

GRB 170817A (also GW170817) became the first binary neutron star merger event detected via gravitational waves and electromagnetic signals. Over the next 4 yr, various multiband observations have led to reimaging of the various short gamma-ray burst and interstellar medium interaction models. While these models successfully explain the observed afterglow until ∼900 days, a rebrightening or excess flux was observed in the 1 keV X-ray band after ∼1000 days. In this study, we reevaluate the jet parameters using new observations (until ∼1234 days) with a boosted fireball jet model. We study the observable effects of the counterjet for GRB 170817A, using our new afterglow code, FIREFLY. Our results show that it is indeed possible for the observed excess to coincide with the emissions from a counterjet (∼800 days). We also computed an empirical scaling law between the jet and counterjet peak emission timescales and the observer angle. The FIREFLY code can also track the simulated object through the observer's sky and numerically model the apparent motion. The calculated apparent motion ($\approx 2.6c$) does not match the observed apparent motion ($5.2c-7.5c$). Hence we conclude that the excess flux of GRB 170817A may not be associated with a counterjet; however, it is not enough to reject this hypothesis from the traditional counterjet visibility timescale, which predicts $\geqslant$5000 days. The apparent motion, combined with the multiband lightcurves, is needed to break the degeneracy between the geometrical parameters and the microphysical parameters of the afterglow.

Unified Astronomy Thesaurus concepts: Gravitational waves (678); Gamma-ray bursts (629); Relativistic jets (1390); High energy astrophysics (739); Hydrodynamics (1963)

1. Introduction

Binary neutron star (BNS) mergers have long been believed to be a strong candidate for multimessenger astrophysics. On 2017 August 17, GW170817 (and GRB 170817A) became the first such event to be detected directly. It provided unprecedented insights into the physical properties of the premerger (gravitational waves) and postmerger (electromagnetic (EM) signal) BNS. The event was quickly localized (D. A. Coulter et al. 2017) to a nearby galaxy at 40.7 Mpc (M. Cantiello et al. 2018). The initial EM spectrum (∼days) was powered by thermal emission from the merger ejecta (also known as a kilonova) and nonthermal synchrotron emission dominated in the X-ray and radio bands.

The early kilonova emission, powered largely by the radioactive decay of heavy chemical elements, was in agreement with theoretical predictions (B. D. Metzger 2017). Meanwhile, the nonthermal emission in the first ∼900 days has been associated with synchrotron emission from a gamma-ray burst (GRB) afterglow due to an ultrarelativistic jet pointing away from us (K. P. Mooley et al. 2018a; G. Ghirlanda et al. 2019; K. Hotokezaka et al. 2019; A. Nathanail et al. 2021). The initial observations during this period did not show any spectral evolution across 9 orders of magnitude of frequency, and they were characterized as synchrotron emission with power-law spectrum $F_\nu \propto \nu^{-(p-1)/2}$, with $p = 2.166 \pm 0.026$ (W. Fong et al. 2019; A. Hajela et al. 2019; E. Troja et al. 2020). More recent observations, after 900 days since the merger, have found evidence for an excess in X-ray emission. The excess X-ray emission was measured at $L_X \approx 5 \times 10^{38}$ erg s^{-1} at 1234 days. However, similar observations at 3 GHz (radio) and 5 keV (X-ray) lacked such a strong excess (E. Troja et al. 2021; A. Hajela et al. 2022).

The GRB afterglow has been studied extensively, and the physical parameters are constrained by several lightcurve and spectral fits (T. Piran 2005; W. Zhang & A. MacFadyen 2009) for $\delta t < 900$ days. Several simple and complex models of jets have also been employed to explain the behavior of synchrotron emission from GRB170817A. Top-hat jet models, formed by angular truncation of a spherical Blandford–McKee blast wave solution (R. D. Blandford & C. F. McKee 1976), cannot account for the mild and steady rise of the nonthermal emission (E. Troja et al. 2017, and references therein). More complex models include a jet-less fireball model (O. S. Salafia et al. 2017; Y. Wu & A. MacFadyen 2018), the choked jet-cocoon model (E. Nakar & T. Piran 2018), and the choked jet-cocoon model with a fast tail (K. Hotokezaka et al. 2018) characterized by a mildly relativistic quasi-spherical outflow. Other models include a structured jet with wide-angle wings viewed off axis (e.g., A. Kathirgamaraju et al. 2017; R. Margutti et al. 2018 and other), like the Gaussian-shaped jet model (E. Troja et al. 2018, and references therein), the successful jet-cocoon model (P. C. Duffell et al. 2018), and the boosted fireball model (Y. Wu & A. MacFadyen 2018). These complex models have been successful in explaining the spectral and temporal evolution of the synchrotron emission from GRB170817A, but in the context of successful jet breakout, they are indistinguishable from each other (Y. Wu & A. MacFadyen 2018, and references therein). However, the lightcurves show significant statistical deviation from the recent X-ray excess observed at 1 keV. This

excess emission has been associated with kilonova ejecta (A. Kathirgamaraju et al. 2019), and also compact object remnants like a hypermassive neutron star (NS), or a prompt collapse to a black hole, or a spinning-down NS (A. Hajela et al. 2022, and references therein).

In this paper, we adopt the boosted fireball model (P. C. Duffell & A. I. MacFadyen 2013). We then revisit the parameter space for the standard external shock and interstellar medium (ISM) interaction model of GRB afterglows (R. Sari et al. 1999; J. Granot & R. Sari 2002) and include the most recent observations (up to <1300 days). One should note that the existing best-fit parameters are based on observations for $\delta t < 900$ days, and the lightcurves deviate beyond that epoch. We compare the reevaluated jet and afterglow microphysical parameters with the existing best fits and Markov Chain Monte Carlo results. Motivated by the association of late-time bumps in afterglow lightcurves to counterjet rebrightening (J. Granot & A. Loeb 2003; Z. Li & L. M. Song 2004; X. Wang et al. 2009; W. Zhang & A. MacFadyen 2009), we revisit this scenario as a probable source of the excess flux in the recent observations of GRB 170817A. We further make predictions for later behavior. We also explore the correlation between the ratio of the global peak flux to the counterjet bump and the observer angle.

The question we ask here is, being agnostic of the observer angle, is it possible to correlate the rebrightening timescale with the emergence of counterjet emissions? If so, what are the required conditions for it? The paper is presented as follows. In Section 2, we discuss the theoretical aspects behind the problem. This is followed by Section 3, which describes the numerical implementations. Here we also introduce our new synchrotron radiation code FIREFLY. This includes how we use FIREFLY to map the flux distribution along the plane perpendicular to the observer's line of sight. We discuss our findings and overall line of thought in Section 4. Section 4.1 discusses the empirical scaling law between the timescales of the forward jet peak emission and the counterjet peak emission. This is followed by a discussion comparing our simulated lightcurves to the observations in Section 4.2 and the spectrum in Section 4.3. Finally, we estimate the apparent superluminal motion for the brightest region of the GRB 170817A afterglow through the sky in Section 4.4. We summarize and discuss our findings and their implication in the conclusions (Section 5).

2. Theoretical Models

In this work, we use the boosted fireball jet model. The boosted fireball is a two-parameter model (P. C. Duffell & A. I. MacFadyen 2013) that generates a family of outflows after they have expanded many orders of magnitude larger than the merger scale. The two input parameters are $\eta_0 \sim E/M$ and the fluid-frame Lorentz factor of a blast with energy E and mass M, where $\gamma_B \sim \frac{1}{\theta_0}$ is the boost (in the lab frame or blast frame) given to said blast and θ_0 is the jet opening angle. In contrast to a conventional fireball which expands isotropically (with the Lorentz factor η, as per our convention), the boosted fireball has gets an external kick in a particular direction with Lorentz factor Γ_B. In the extreme limit $\Gamma_B \to 1$, the boosted fireball is the same as a conventional fireball. While on the other end for $\Gamma_B \to \infty$ it corresponds to an ultrarelativistic jet with a negligible jet opening angle ($\theta_0 \approx 1/\Gamma_B$). The explosion energy per fireball is $E_0 \sim \gamma_B \eta_0 E$. Thus for a double-sided jet, the total energy will be $2E_0$, which is related to the isotropic equivalent energy ($E_{\rm iso}$) by the relation

$$2E_0 \simeq 4\pi(\theta_0)^2 \frac{dE}{d\Omega} \sim \frac{E_{iso}}{\gamma_B^2}. \quad (1)$$

A single fireball has previously been used to simulate the forward jet, and its dynamics are comparable to other standard jet models (Y. Wu & A. MacFadyen 2018). In this work we consider two symmetrically reflected fireballs along the jet axis, but they are boosted in opposite directions. This simulates the joint evolution of the forward jet and the counterjet. We assume a constant and equal boost in both directions. This is justified because the merger's spatial and temporal scales are much smaller than the afterglow's spatial and temporal scales.

For this study, we have used the standard GRB afterglow theory (R. Sari et al. 1998; J. Granot & R. Sari 2002). This refers to models based on synchrotron radiation from a decelerating relativistic blast wave interacting with the ISM. It assumes the radiation is generated by nonthermally distributed electrons accelerated by a forward shock. These electrons are further assumed to be distributed as a power law of their Lorentz factor $n_e' = C_e f n' {\gamma_e}'^{-p}$, where $\gamma_e' > \gamma_m'$ (H. van Eerten 2013), where primed quantities are expressed in the fluid comoving frame, and f is the fraction of electrons radiating (n'). Assuming electrons are accelerated to $\gamma_{\mathscr{e}} \to \infty$ this equation can be integrated to obtain the normalization constant C_e as $C_e = \frac{1}{f}(p-1)\gamma_m^{p-1}$. We found a marginal change in f has no significant effect on the lightcurves. It was hence fixed at one for the rest of the analysis. The minimum electron Lorentz factor at which the accelerated electrons are radiating (γ_m') is given by Equation (5). Similarly, the cooling break can be solved as in Equation (7), where ϵ_e and ϵ_B are the fraction of total energy ($\epsilon_{\rm th}$) converted to kinetic and magnetic energy, respectively. Further, due to the relativistic nature of the blast wave, most of the density is concentrated in a very thin shell behind the forward shock. The radiation is dominated by electrons present in this shocked shell of width $\Delta R/R \sim 1/(12\Gamma^2)$, where Γ is the jet head Lorentz factor

$$\epsilon_B = \frac{B'^2}{8\pi e_{\rm th}'}, \quad (2)$$

$$\epsilon_e = \frac{\int n_e' \gamma_e' m_e c^2 d\gamma_e'}{e_{\rm th}'}. \quad (3)$$

The quantities upstream (ahead of the shock, in the ISM) and downstream of the shock are related as $n'_e = 4\Gamma n_e$ and $e'_{\rm th} = (\Gamma - 1) n'_e m_p c^2$. Thus the above equation after integrating and some algebra, can be solved to give

$$B' = \sqrt{32\pi\Gamma(\Gamma-1) n_e m_p \epsilon_B c^2}, \quad (4)$$

and

$$\gamma_m' = \frac{p-2}{p-1}\frac{\epsilon_e m_p}{f m_e}(\Gamma - 1). \quad (5)$$

The corresponding break frequencies can be found using Equation (6)

$$\nu_i{}' = \frac{3eB'\gamma_e'^2}{4\pi m_e c}. \quad (6)$$

Here, γ_i' is the Lorentz factor in the local fluid frame and i corresponds to either cooling break or minimum Lorentz factor

cutoff. However beyond a certain critical Lorentz factor (γ_c'), the electrons starts losing energy by cooling over timescale t' (in lab frame $t = \gamma t'$). The frequency at which this happens is hence called the cooling frequency, ν_c'. This can be estimated by equating the power lost over some expansion time (t) to the rest mass energy, and it comes out to be (see H. van Eerten et al. 2010 for detailed calculations)

$$\gamma_c' = \frac{6\pi m_e \gamma c}{\sigma_T B'^2 t}. \tag{7}$$

The characteristic frequencies, ν_m and ν_c, can be observed as two break frequencies in the spectrum. Thus in the local fluid frame, a given fluid element has monochromatic emissivity per unit volume

$$\epsilon'_{\nu'} = \epsilon'_p \times \begin{cases} (\nu'/\nu'_m)^{1/3} & \text{if } \nu' < \nu'_m < \nu'_c, \\ (\nu'/\nu'_m)^{-(p-1)/2} & \text{if } \nu'_m < \nu' < \nu'_c, \\ (\nu'_c/\nu'_m)^{-(p-1)/2}(\nu'/\nu'_c)^{-p/2} & \text{if } \nu'_m < \nu'_c < \nu', \\ (\nu'/\nu'_c)^{1/3} & \text{if } \nu' < \nu'_c < \nu'_m, \\ (\nu'/\nu'_c)^{-1/2} & \text{if } \nu'_c < \nu' < \nu'_m, \\ (\nu'_m/\nu'_c)^{-1/2}(\nu'/\nu'_m)^{-p/2} & \text{if } \nu'_c < \nu'_m < \nu', \end{cases} \tag{8}$$

where

$$\epsilon'_p = \frac{\sqrt{3}\, e^3 B' f n'}{m_e c^2}. \tag{9}$$

Since most of the mass in a relativistic blast wave is concentrated in a very thin shell behind the shock, the observed emission comes only from this optically thin shell. This has a volume element given by

$$dV = R^2 \sin\theta dR d\theta d\phi. \tag{10}$$

This converts to observed flux from the lab frame for a fluid element having Doppler factor δ as

$$F_\nu(\nu, t_{\rm obs}) = \frac{1+z}{4\pi D_L^2} \int \epsilon'_{\nu'} \times \delta^2 \times dV. \tag{11}$$

Here, z is the cosmological redshift and D_L is the luminosity distance of the source. The local fluid-frame frequency (ν') and time (t') are related to the observer frequency ($\nu_{\rm obs}$) and observer time ($t_{\rm obs}$) as

$$\nu_{\rm obs} = \frac{\delta}{1+z}\nu', \tag{12}$$

$$\frac{t_{\rm obs}}{(1+z)} = t' - \frac{\vec{r}' \cdot \hat{n}}{c}. \tag{13}$$

At any given time and frequency, the observed flux is a result of the total light collected from all the photons arriving at the same time to the observer. In the lab frame (or the center of blast frame), these contours are known as equal arrival time surfaces and are spread over the entire jet at all times. The two frames, lab frame and observer frame, can be bridged by taking a projection of the local fluid element ($\boldsymbol{r}$) (with respect to the center of blast), along the line of sight of the observer ($\hat{n}$)

$$\delta = \Gamma^{-1}(1 - \boldsymbol{v} \cdot \hat{n})^{-1}. \tag{14}$$

3. Numerical Implementation

The entire process of generating lightcurves and spectra from jets can be divided into two parts. First we hydrodynamically evolve two oppositely directed relativistic jets through a constant density ISM originating from the center of our domain. The domain is assumed to be in the BNS merger rest frame, and the fireballs are boosted with respect to this frame by Lorentzian transformations (see P. C. Duffell & A. I. MacFadyen 2013 for the detailed calculations). This was carried out using the two-dimensional relativistic hydrodynamics moving mesh code JET (P. C. Duffell et al. 2018).

Each jet is initiated as a boosted fireball with a given fluid-frame Lorentz factor η_0 and boosted with a Lorentz factor γ_B. The hydrodynamic simulations are carried out in code units normalized by setting the Sedov radius, $l \equiv (E/\rho_0)^{1/3}$, to unity in the center of blast frame. This translates to the total blast energy E and a constant ISM density (ρ_0) set to unity. These are scaled to physical units during the afterglow calculations. The input for $\eta_0 \sim E/M$ sets the total ejected mass in the jet, and $\gamma_B \sim 1/\theta_0$ sets the jet opening angle (θ_0), both in code units. The simulation begins around the time the fireball enters the Blandford–McKee self-similar phase, $t_{\rm BM} \sim (E/(\rho_0 c^5 \Gamma^2))^{1/3}$, which sets the initial time $t_{\rm min} = 0.06 t_{\rm BM}$ (where $c = 1$ in code units). This ensures that the blast wave evolution begins before the radiation is dominated by the ejecta swept up by the forward shock. The system is evolved until it expands to 20 times its Sedov radius (that is, $t_{\rm final} = 20l/c$), where it becomes subrelativistic. The system stratifies to a density profile given by Equation (15). A homologous expansion of the ejecta ($v = r/t$) is assumed

$$\rho(r) = \rho_{\rm max}\left(\frac{1 - R_{\rm sh}/t}{1 - r/t}\right), \tag{15}$$

$$v(r, t) = \begin{cases} r/t & \text{if } v < R_{\rm sh}, \\ 0 & \text{otherwise}, \end{cases} \tag{16}$$

$$P \ll \rho. \tag{17}$$

Here, $\rho_{\rm max} \sim E/4\pi c^3 t^3$ is the maximum blast wave density at the shock and follows from $E = 4\pi\rho_{\rm max}(ct)^3 c^2$. The shock radius ($R_{\rm sh}$) is given by $R_{\rm sh} = t(1 - 1/2\eta_0^2)$. The pressure is set to be very low ($10^{-5}\rho$) initially. An adiabatic equation of state is used with a constant adiabatic index of 4/3 for relativistic fluids. Although, by the end of our simulation the flow becomes subrelativistic, the afterglow emissions are dominant in the relativistic phase. The relativistic adiabatic constant holds true for a marginally relativistic flow as well. Hence, a single value for the adiabatic constant does not affect the results significantly. The counterjet is implemented by reflecting the forward jet about the plane perpendicular to the jet axis. Lastly, the fireball is expanded in an ISM of constant density normalized to unity. A snapshot of the evolution is shown in Figure 1.

Since the problem is axisymmetric, the domain is set in a two-dimensional $r-\theta$ plane polar mesh. The θ coordinate varies from 0 to π, and is split into 3200 zones. The radial coordinate is initiated with $R_{\rm min} = 0.006\, l$ and $R_{\rm max} = 0.061\, l$, and is split into 6400 zones. These resolutions capture both the radial and angular features well enough keeping the run time feasible. A smaller initial radial domain (as compared to the entire radial range of the problem) helps capture the shock at a higher Lorentz factor. The radial mesh eventually expands, moving the inner and outer boundaries using the moving mesh feature of the JET code, and dynamically captures the entire radial range of the jets with temporal evolution. This is achieved by fixing the ratio of the inner to outer domain with respect to the shock front. We use

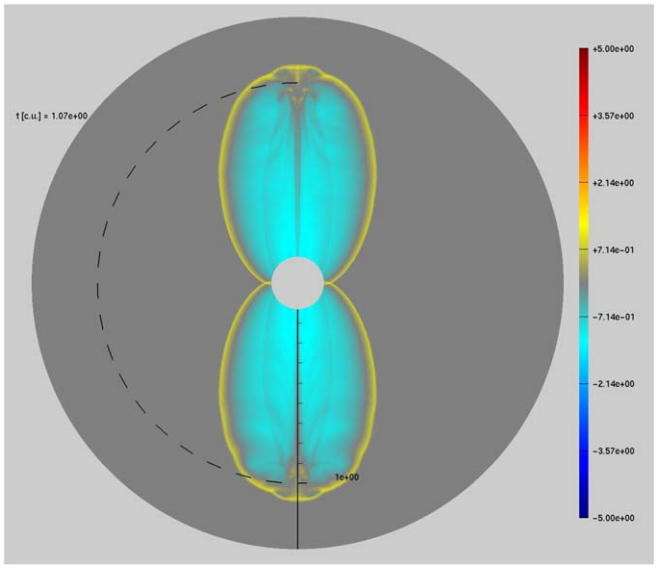

Figure 1. Density snapshot of our jet–counterjet model using the JET code. Two opposing boosted fireballs are injected, each with a single impulse normalized energy. The jets are evolving through a constant density medium, $n_{\rm ISM} = 0.1$ cm^{-3}, marked by the gray background. The dashed black circle is for scaling reference, which marks the radial distance $r = 1.07$ [code units] $\approx 2.53 \times 10^{18}$ cm. The snapshot is the density profile at a typical time during its evolution.

a logarithmic time grid varying from 0.06 code units to 20 code units split in 10^5 time steps.

We developed a code, FIREFLY, to postprocess the hydro simulations from the JET code. The FIREFLY code takes the complete two-dimensional hydrodynamical evolution as its input and computes the three-dimensional synchrotron radiation using the standard afterglow model as described in the previous section. The 2D hydro data are extended to three dimensions by FIREFLY using the rotational symmetry about the jet axis. The radial and θ resolutions for the afterglow calculations assume the same resolution as the JET code output, while the ϕ axis is divided into 64 zones from 0 to π. The hydrodynamical parameters thus have the same value for all ϕ zones at a given (r, θ). The hydro checkpoints are then binned over temporal resolution for the observer $t_{\rm obs}/dt_{\rm obs} = 0.03$. The binning ratio is a user choice; we choose the mentioned ratio to generate a smooth lightcurve without the loss of any physical features. FIREFLY has three user input modes: to calculate the lightcurve, spectrum, or sky map. For each mode, it takes the total energy ($E_{\rm tot}$), interstellar nucleon density ($n_{\rm ISM}$), which is the same as n_e in Section 2, and other microphysical parameters (ϵ_B, ϵ_e, and spectral index p) as user inputs. The total energy for a two-jet system is related to the isotropic equivalent energy by Equation (18). The quantities $E_{\rm tot}$ and $n_{\rm ISM}$ are scaled in the FIREFLY code as their code unit values in the hydrodynamical evolution. Since in the JET code these values are scaled to unity in code units, the input values in the FIREFLY code are the absolute values (corresponding to actual units, i.e., cgs or SI) pertaining to the problem. An observer is placed at luminosity distance (d_L) with a redshift (z) at an angle $\theta_{\rm obs}$. FIREFLY can then be used to calculate the lightcurve (at any given observer frequency). FIREFLY computes the cooling break and minimum break frequencies to correctly generate the broken power-law spectrum of the GRB afterglow. It however does not account

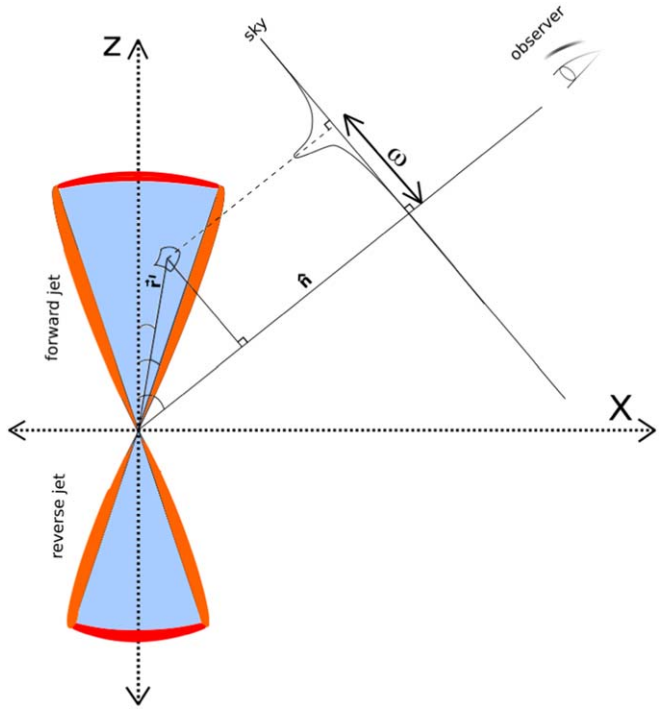

Figure 2. Pictorial representation of the sky map calculation. Contributions from a particular emission region ($\hat{\boldsymbol{r}}$) along the line of sight ($\hat{\boldsymbol{n}}$) are considered, and integrated over the entire domain. The line of sight is fixed at an angle of $\theta_{\rm obs}$. Its flux at the observer plane at $d_L \approx 40$ Mpc from the merger is calculated.

for synchrotron self-absorption

$$E_{\rm tot} = \frac{\theta_0^2}{2} E_{\rm iso}. \tag{18}$$

Additionally, FIREFLY can also be used to track the apparent motion of the object in the sky (as seen by the observer). This is achieved by computing the flux distribution (for a user-given frequency) along a plane perpendicular to the line of sight of the observer and the merger (hereon referred to as a sky map, see Figure 2), as a function of its distance from the merger center. This provides a more realistic approach to tracking the entire shock–ISM interaction region through the sky, and not just the jet head. This is especially relevant for off-axis observations and structured jets. The brightest emitting region from such a plot at multiple observer times can then be used to calculate the apparent motion of the object through the sky.

The sky map is computed by integrating the projected flux along a line on the plane perpendicular to the observer axis from different emitting regions of the jet–ISM interaction. To do this, we consider the x–z plane containing the jet axis and observer. A small emitting region of the jet at $\boldsymbol{r}$ from the blast center is projected on this plane containing the jet axis and the vector ($\hat{n}$), connecting the blast center and the observer, by removing the $\hat{y}$-component (axis into the plane of the paper). This gives the position vector of the projected region

$$\boldsymbol{r} = \boldsymbol{r} - (\boldsymbol{r} \cdot \hat{y})\hat{y}. \tag{19}$$

We then calculate its shortest distance (ω) along the plane perpendicular to $\hat{n}$. This is given by the cross product of the remaining vector with the observer axis ($\hat{n}$)

$$\boldsymbol{\omega} = \boldsymbol{r} \times \hat{n}.$$

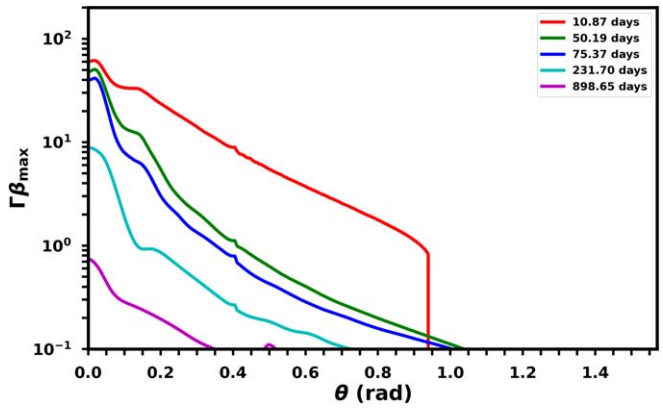

Figure 3. The four-velocity evolution of the fireball. The red curve reflects the angular profile in the beginning of the simulation. The following colored plots are at various epochs under consideration in this paper. The boosted fireball starts with a narrow opening angle θ_{obs} $1/\Gamma_B$ 0.25 rad. It then spreads out as the fireball evolves.

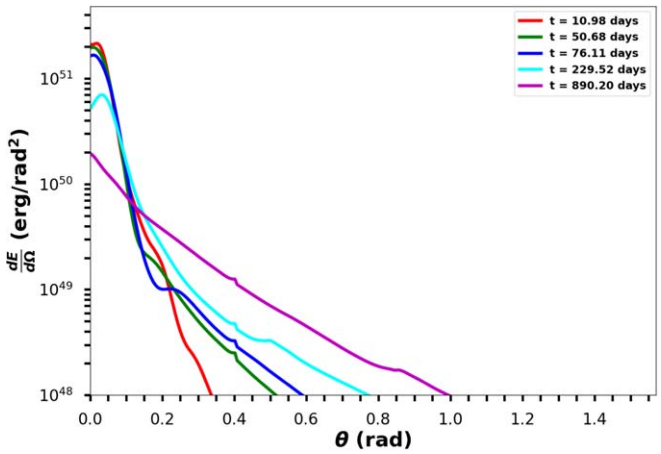

Figure 4. The same as Figure 3. This figure shows the evolution of the boosted fireball energy profile. The energy per unit solid angle is plotted at various epochs.

Since the resulting quantity is a vector, we project it along $\hat{y}$. The geometry can be expressed mathematically as Equation (20), and pictorially as Figure 2. This scheme is then repeated over the entire computation domain at a given observer time

$$\omega = \{[\vec{r} - (\vec{r} \cdot \hat{y})\hat{y}] \times \hat{n}\} \cdot \hat{y}. \quad (20)$$

4. Results

For this study, we explore the parameter space containing E_{iso}, γ_B, η_0, θ_{obs}, n_{ISM}, p, ϵ_e, and ϵ_B. We carried out several runs of the hydrodynamical code for the boosted fireball model (P. C. Duffell & A. I. MacFadyen 2013) varying η_0, and γ_B. Values were selected from a parameter range of $\eta_0 \in [4, 12]$ and $\gamma_B \in [4, 12]$ (inspired by Y. Wu & A. MacFadyen 2018). The temporal evolution of the angular energy profile and Lorentz factor for the fireball are plotted in Figures 3 and 4, respectively. We fixed the luminosity distance $d_L = 40$ Mpc, which corresponds to a cosmological redshift of $z = 0.00998$. Since the Blandford–McKee solution for a relativistic blast wave holds for most of the evolution, we fix the adiabatic index to $4/3$.

For a given set of hydrodynamics parameters, we fix all the microphysical afterglow parameters except θ_{obs} and generate lightcurves as in Figure 5. We observe a late-time bump in the lightcurves due to the counterjet as expected (J. Granot & A. Loeb 2003; Z. Li & L. M. Song 2004; F.-W. Zhang et al. 2013; L.-B. Li et al. 2019). The counterjet excess flux of the afterglow lightcurves indicates a similar rebrightening timescale for off-axis observations, except for far off axis ($\gtrsim$1.2 rad). For these large off-axis observer angles, the rebrightening initiates at earlier times. Figure 5 shows the same. This also shows that the second bump is indeed associated with the counterjet. Emission from the counterjet shares the same profile in the afterglow lightcurve as the forward jet, but with a very significantly delayed t_{obs}, due to its orientation pointing and moving away from the observer. While all of the initial afterglow is due to the forward jet, once the jet spreads out and is spherical enough, the counterjet eventually becomes visible to the observer. Flux from the counterjet gradually increases as the forward jet did, and it eventually outshines the forward jet. This occurs because the observer time t_{obs} for the counterjet corresponds to an earlier lab-frame time than for the forward jet. The forward jet eventually spreads out and

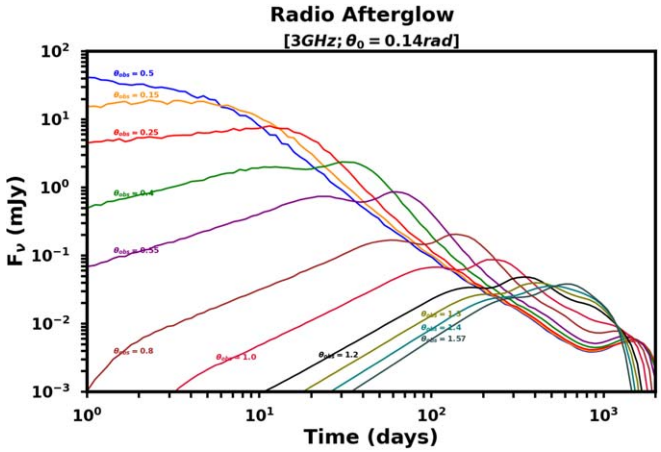

Figure 5. Lightcurves for a given set of jet–ISM parameters, but varying the observer angle. The lightcurves for observer angles $\theta_{obs} = [0.5, 0.15, 0.25, 0.40, 0.55, 0.80, 1.00, 1.20, 1.30, 1.40, 1.57]$ rad are shown. For $\theta_{obs} < \theta_0 (=0.14$ rad), we see the lightcurves start with a plateau-like feature. For larger viewing angles ($\theta_{obs} > \theta_0$), the lightcurve increases first, due to emissions from the jet limbs. As the jet slows down and spreads, the jet core eventually becomes visible, and the lightcurve peaks. Irrespective of the observer angle, the second rise and peak are due to the counterjet happening almost at the same time around 1000 days. For extreme off-axis angles ($\theta_{obs} > 1.2$ rad), we enter a regime when the forward and counterjets cannot be distinguished from each other. This results in single peak lightcurves. These lightcurves peak at a much later time, closer to the second rebrightening, and fall off sharply almost immediately.

slows down, leading to a steeply declining lightcurve, while the counterjet is still effectively beamed and relativistic at the same observer time. For a brief period, this leads to a higher flux from the counterjet. This effect is also captured in the sky map at ~900 days, Figure 6. The flux from the counterjet also eventually peaks and is briefly brighter than the forward jet before it declines. The flux from both jets converges asymptotically and eventually contributes the same amount of emission as the jets spread and eventually become an isotropic system.

4.1. Counterjet Time

While all of the initial afterglow is due to the forward jet, once the jet spreads out and is spherical enough, the counterjet

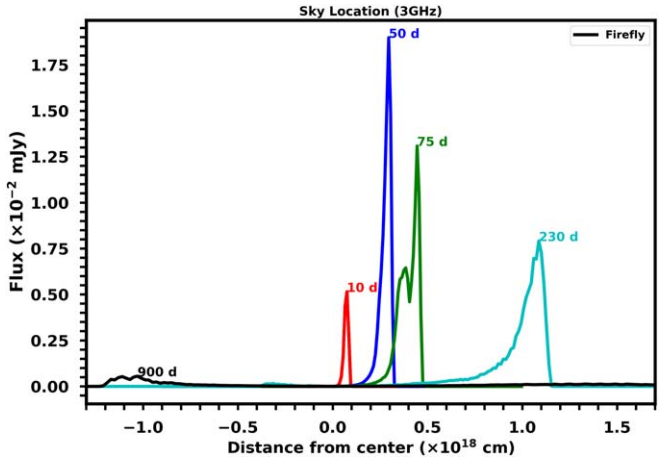

Figure 6. Flux sky map for a boosted fireball model, generated using the FIREFLY code. We have plotted the flux distribution along the plane perpendicular to the observer. The zero on the x-axis denotes the merger center. The flux map starts as sharp and near the merger. Around 900 days, the dominant region appears to come from behind the merger, a little over 10^{18} cm away from the center. This shows the emergence of the counterjet. The sky flux map is drawn for five instances in time: 10, 50, 75, 230, and 900 days.

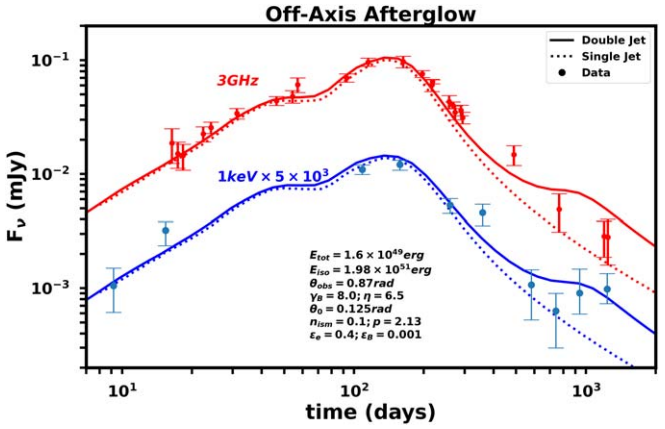

Figure 7. Lightcurves at 3 GHz (red) and 1 keV (blue) for GRB 170817A as observed from $\theta_{\rm obs} = 49.^{\circ}8$. The solid circles are data taken from various sources listed in the text. The solid and dashed lines are lightcurves with and without the counterjet, respectively. The clear late-time excess seen in the solid lines, compared to the dashed line, implies the excess emissions come from a counterjet, peaking around 1000 days. The excess flux seen in the data, especially for the 1 keV X-ray band, matches very closely with the counterjet rebrightening within the errors of the observations. But a stronger emission is expected at 3 GHz around the rebrightening time.

eventually becomes visible to the observer. This can be seen as a late-time bump in the afterglow lightcurves (J. Granot & A. Loeb 2003; Z. Li & L. M. Song 2004; F.-W. Zhang et al. 2013; L.-B. Li et al. 2019), and Figure 7. L.-B. Li et al. (2019) and A. Hajela et al. (2022) give an estimate of the counterjet visibility time as

$$t_{cj} \approx (1+z)t_{\rm NR} \approx 1900(1+z)(E_{\rm iso,53}/n_0)^{1/3}{\rm days}. \quad (21)$$

It must be noted here that since we are off axis from the jet core, we do not need the entire jet and counterjet to be completely spherical for the counterjet to become visible. We model the timescale for the counterjet peak emission (t_p^{cj}), in terms of the timescale of the forward jet peak emission(t_p^{j}), and the observer angle ($\theta_{\rm obs}$).

For a given observer angle at a given frequency, we identify the time and flux from the two peaks due to the forward and counterjet from the lightcurve. We then carried out a parametric study of the temporal ratio of these two epochs over the range $\theta_{\rm obs} \in [0, \frac{\pi}{2}]$. The results are shown in Figure 8. The same scheme is used for two different frequencies/energies, 3 GHz and 1 keV, to study the chromatic dependence as well.

We find that the temporal peak ratios have achromatic behavior. That is, the timescale relations between the jet and counterjet peak emission should be valid for all frequencies. For an on-axis observer, within the jet opening angle θ_0 ($>\theta_{\rm obs}$), the forward jet peak time is the earliest observer time, hence the ratio $t_p^j/t_p^{cj} \ll 1$. While on the other extreme for a far off-axis observer, $\theta_{\rm obs} \gg \theta_0$, the forward and counterjet are indistinguishable, and the ratio $t_p^j/t_p^{cj} \approx 1$. That is, the total emission is equally contributed by both the jets, leading up to a single peak. In between, for an off-axis observer $\theta_{\rm obs} > \theta_0$ ($\theta_{\rm obs} \approx \pi/2$), the peak flux from the forward jet gradually moves toward the peak from the counterjet as we go further off axis. This is shown in Figure 5. In this regime, assuming γ_B, η_0, and ISM remain fixed, we can fit a curve relating the peak time ratios to the observer angle as

$$\frac{t_p^j}{t_p^{cj}} = \left[\frac{\theta_{\rm obs}}{\pi - \theta_{\rm obs}}\right]^{2.07}. \quad (22)$$

With $t_p^j = 175$ days, and assuming the counterjet peak emission is later than 1234 days, we can place a lower bound of $\frac{t_p^j}{t_p^{cj}} > 10^{-0.85}$ from the observations. Using our scaling law in Equation (22), this gives $\theta_{\rm obs} \approx 49.^{\circ}8$.

The ratio of fluxes at t_p^j and t_p^{cj} do not follow such a simple relationship. Since the flux is also dependent on the break frequencies, the flux ratio at the jet–counterjet peak epochs need not be achromatic. Rather they should depend strongly on the spectral breaks. In the particular case of GRB 170817A, the spectral index maintains a rather fixed value, they happen to align.

4.2. Lightcurve

Since GRB 170817A was observed off axis, the lightcurve rises and peaks around 160 days. This is because early emissions arise from the off-axis jet material, and higher-energy material continues to come into view as the jet decelerates. The lightcurve peaks when the jet core becomes visible to the observer. The flux starts to decline thereafter. This is due to the fact the jet slows down and loses energy as it expands. Up until this point, the radiation is dominated by the forward jet oriented toward us. Hydro simulations with a single jet or double jet cannot be distinguished from their afterglows until much later.

The lightcurves are constructed using the standard afterglow theory detailed in previous sections. We use our code FIREFLY for this. We construct various lightcurves and constrain the afterglow microphysical parameters with the observations at $\theta_{\rm obs} \approx 49.^{\circ}8$. We find the best match for the parameters reported in Table 1. Taking into account the recent observations ($t_{\rm obs} > 900$ days) we find that the excess flux observed could be associated with the counterjet rebrightening for GRB 170817A, if one only considers the lightcurve.

We focus our results mainly at two frequencies/energies, X-ray at 1 keV and the 3 GHz radio band. The frequencies are chosen to compare our results with the observations reported in

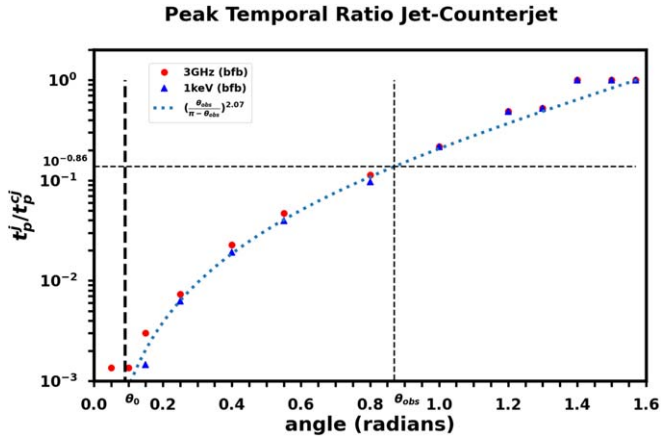

Figure 8. Ratios of the timescales when the emissions from the forward jet peak, to that of the counterjet on the y-axis, compared to the observer angle along the x-axis. This is measured at two frequencies/energies: the 3 GHz radio band and 1 keV X-ray band. We find no difference in their dependence on the observer angle, as expected. This temporal ratio follows the empirical scaling law in Equation (22). This is plotted as blue dashed lines. The region of interest is when $t_p^j/t_p^{cj} \sim 175/1234$, which is the prospective observer viewing angle $\theta_{\rm obs} \sim 0.85$ rad, which is also marked with thin black dashed lines. The thick dashed line at $\theta_0 = 0.09$ rad shows the jet opening angle. Due to various shocks and numerical instabilities at the jet wing boundaries, the temporal ratio is slightly different for the X-ray and radio near the jet opening angle. Since $\theta_{\rm obs}$ is much greater than the jet opening angle, this numerical effect can be ignored without loss of generality.

Table 1
Parameter Range for the Fireball Jet

Parameter	Double Fireball
γ_B	8.0
η_0	6.5
θ_0	7.°2
$E_{\rm tot}$	1.6×10^{49} erg
E_{iso}	1.98×10^{51} erg
$\theta_{\rm obs}$	49.°8
$n_{\rm ISM}$	0.1 cm^{-3}
p	2.13
ϵ_e	0.4
ϵ_B	10^{-3}

Note. There are eight free parameters in the boosted fireball afterglow model. The first two are for the jet itself for the boosted fireball model (γ_B and η_0). The remaining six parameters come from the standard afterglow model. Their parameter ranges are chosen according to the physical limits set on them. These are the values for which we find the best agreement between the 3 GHz and 1 keV lightcurve. These are the parameters required to correlate the 1 keV excess flux to the counterjet emission for GRB 170817. The most notable differences to previous studies are the values of $n_{\rm ISM}$, and $\theta_{\rm obs}$.

E. Troja et al. (20210 and A. Hajela et al. (2022). Figure 7 shows the comparison. A. Hajela et al. (2022) and the models discussed therein, use the afterglow observations until 700 days to constrain the jet and its afterglow parameters.

Figure 7 shows that it is possible to explain the excess flux observed for GRB 170817A, as emissions originating from the counterjet. It also shows how the lightcurve would look if only a single forward jet was considered. The main deviation from the previously accepted set of parameter values for the short GRB (sGRB) jet is in the observer angle. We find a far off-axis observer is needed to explain the early rebrightening from a counterjet. We find an observer located at 49.°85, along with the set of parameters reported in Table 1, would observe the emissions from a counterjet at around 1234 days at 1 keV, coincident with the excess flux. Along with the same lightcurve for previous times.

While the agreement with the 1 keV lightcurve is convincing, we see around the same time the 3 GHz lightcurve does not show a significant excess in flux. As we previously argued, we expect the counterjet rebrightening of the system should be seen across all frequencies. One explanation can be that by this time, the synchrotron self-absorption break lies beyond 3 GHz. It is possible that the emissions below the self-absorption break from the counterjet might also undergo more loss, diminishing its contribution as compared to the forward jet. This is due to the fact the emissions experience more ISM interaction as they pass through both the counterjet and jet lobes, unlike the emissions below the self-absorption frequency from the forward jet, which get self-absorbed only in the forward jet lobe. We find this break using Equation (23) to be 3.6×10^8 Hz around $t_d \sim 1000$ days. This does not explain the lower flux observed at 3 GHz, compared to the predictions from the counterjet model (Figure 7). We note that this discrepancy thus still remains. However, E. Troja et al. (2021) found no such excess flux in the 5 keV band as well.

4.3. Spectrum

Along with the afterglow, the spectrum of GRB 170817A has been closely observed. The power-law index p characterizing this spectrum is expected to evolve as the blast wave transitions from a highly relativistic to nonrelativistic regime (A. R. Bell 1978; R. D. Blandford & J. P. Ostriker 1978). However, no such major variation has been seen (A. Hajela et al. 2022). Thus, all models so far have assumed a fixed p value (Y. Wu & A. MacFadyen 2018; E. Troja et al. 2021; A. Hajela et al. 2022, and references therein). Reevaluation of values of $p > 2.166$, i.e., larger than the best-fit value for $t < 900$ days can be ruled out (A. Hajela et al. 2022).

For our study, we assume a nonevolving value of p. We fix the parameters from the afterglow and we generate the corresponding spectrum using our code FIREFLY. FIREFLY however does not include synchrotron self-absorption.

We find the best fit at $p = 2.13$. This is similar to other results from the boosted fireball model, e.g., $p = 2.154$ reported by Y. Wu & A. MacFadyen (2018) and is approximately the same as $p = 2.166 \pm 0.026$ from the latest epochs (E. Troja et al. 2021; A. Hajela et al. 2022). Another notable feature of the spectrum is the same power-law behavior over the entire spectrum from radio to X-ray. That is, none of the frequency breaks lie within the range 3×10^6 Hz to 3×10^{17} Hz. While synchrotron self-absorption is not captured in our code, we estimated the value to be around 3.6×10^8 Hz following Equation (23) (J. Granot & R. Sari 2002), which lies below the frequency range of our interest

$$\nu_a = 3.59(4.03 - p)e^{2.34p}\left(\frac{\epsilon_e^{4(1-p)}\epsilon_B^{p+2}n_0^4E_{52}^{p+2}}{(1+z)^{(6-p)}t_d^{3p+2}}\right)^{\frac{1}{2(p+4)}}\text{Hz}. \quad (23)$$

It must be noted at this point that our parameters were chosen such that we can coincide the excess flux observed for

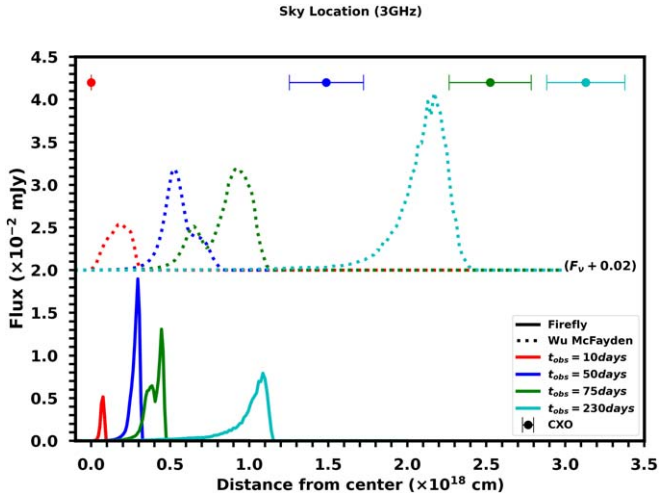

Figure 9. The location of the maximum emitting region at 3 GHz for the off-axis jet of GRB 170817A is plotted. The observer is placed at $\theta_{\rm obs} = 0.87$ rad. Plotted at the top (the solid circles) is the observed physical distance of the merger center to the maximum emitting region on the sky at 3 GHz, from K. P. Mooley et al. (2018a). Plotted below that is the flux map at the different epochs. These show the apparent motion of the flux contributions from the afterglow, along the line joining the merger center and the observer. The solid lines are obtained using the parameters from this paper (Table 1) while the dashed lines are obtained using the Y. Wu & A. MacFadyen (2018) model. The peaks from these plots are used to identify the location of GRB 170817A for that given time.

GRB 170817A, with the rise of counterjet emission. While this may seem an ad hoc way of parameter estimation, our parameters are well within the permissible limits of the microphysics behind the afterglow theory.

4.4. Apparent Motion

Using the sky map feature of our FIREFLY code, we plot the flux versus sky location. Figure 9 shows this output at various observer times when observed at 3 GHz. For a given time (say the blue curve in Figure 9), we see a narrow profile with a sharp peak. The peak represents the brightest spot for the GRB 170817A afterglow in the sky, and hence its observed distance from the merger center. Over time the profile spreads out and moves away from the merger center. The flux at the peak also decreases with time and follows the lightcurve. The spread in the profile is directly correlated with the increase in shock width as the jet spreads and decelerates ($\Delta R \sim 1/\Gamma^2$).

Eventually, at a later time of ∼900 days, we see the maximum flux in the opposite direction, as if the jet switches its location. This is from the now brighter counterjet, which is still beamed and relativistic. The exact time at which this happens depends on the observer angle as discussed previously. This is in agreement with our previous argument that the late-time excess flux is primarily due to the counterjet.

For now, we consider the epochs before such an excess flux. Taking the peak as the jet location corresponding to that time, we can calculate the apparent motion from Figure 9 directly. Table 2 summarizes the results for the apparent motion. We find the apparent velocity remains superluminal even at 230 days. However, the apparent velocity decreases from 2.1c to 1.6c for the first 200 days since the BNS merger.

Our inferred superluminal motion conflicts with observations. The apparent motion is highly sensitive to the observer angle: G. Ryan et al. (2023) and K. P. Mooley et al. (2018a) observed a superluminal apparent velocity of 7 times the speed of light for GRB 170817A, even after a year. Centroid-corrected fits for the apparent motion give $\theta_{\rm obs} \sim 20^\circ$ for jet opening angle $\sim 3.^\circ5$ (G. Ryan et al. 2023). This hints at a smaller observer angle than what our model predicts. Since the superluminal motion observations are a direct result of the orientation of the jet with respect to the observer, we put a stronger emphasis on the observed motion and its consequences.

Table 2
Apparent Motion of GRB 170817A Determined with FIREFLY

Time Since Merge (days)	Distance from Merger Center ($\times 10^{16}$ cm)	Apparent Velocity (cm s^{-1})
10	7.5	⋯
50	29.5	2.122c
75	44.5	2.354c
230	108.7	1.6c

Note. This table summarizes the apparent motion for our boosted fireball model jet, following the parameters mentioned in Table 1. The third column is the calculated apparent motion, in terms of speed of light c, calculated between the two epochs mentioned in the first column.

Y. Wu & A. MacFadyen (2018) did not compute the apparent motion of the jet with time for their models. However, we reran their setup using the parameter values from their best-fit model, to determine the superluminal motion for the Y. Wu & A. MacFadyen (2018) setup. This is also shown in Figure 9. For the setup of Y. Wu & A. MacFadyen (2018), we see an improved match for the apparent velocity with a smaller observer angle. However, Figure 9 suggests that their setup is also inconsistent with the data, suggesting that a viewing angle even smaller than $26.^\circ9$ may be necessary to match all available data.

5. Conclusion

GRB 170817A is one of the most crucial transients in recent years. While it was the first off-axis sGRB afterglow observed it has reignited multiple questions in the field of GRBs and afterglows. The afterglow from GRB 170817A has also shown a significant agreement with a structured jet interaction with a constant ISM. In this study, we reevaluated the parameters to investigate the conditions under which the observed excess flux could be due to a counterjet.

We ran multiple hydrodynamic simulations for a double-sided boosted fireball jet model, varying γ_B, and η_0. The first peak in the afterglow lightcurves was used to constrain the jet opening angle at $\theta_0 = 1/\gamma_B = 0.125$ rad ($\gamma_B = 8.0$). The fireball spread parameter, quantified by η_0, was similarly constrained to be 6.5. Y. Wu & A. MacFadyen (2018) find an asymptotic Lorentz factor $\gamma_B \sim 11$ and $\eta_0 \sim 8$ (Figure 9). Fixing γ_B and η_0, we constructed lightcurves at 3 GHz (radio) and 1 keV (X-ray) for 11 observer angles each. In our model, there is no additional source of excess flux. Thus the second peak observed in Figure 7 is purely due to counterjet interactions. We also observe that at later times, since the counterjet has a longer $t_{\rm obs}$, it becomes brighter than the forward jet. After this turnover time, the contributions from the counterjet lead to the second peak in the lightcurves. We then computed an empirical scaling

law between the jet and counterjet peak emission timescales, with the observer angle (Equation (22)).

For the excess flux of GRB 170817A to correspond with the emissions from a counterjet, we can place a lower bound of $\frac{t_p^j}{t_p^{cj}} > 10^{-0.85}$ from observations (Section 4.1). Comparing simulations with the observations (Figure 7) we constrain our observer angle to be 49°.8. In contrast, previous attempts studies have found $\theta_{\rm obs} \sim 27°$ (D. Lazzati et al. 2018; K. P. Mooley et al. 2018b; L. Resmi et al. 2018; Y. Wu & A. MacFadyen 2018). Using Equation (22) we estimate the peak of this second component to occur around 1268 days since explosion. The afterglow lightcurve shall then decay sharply, with a temporal slope faster than before the excess started.

Using this observer angle, we fit the 3 GHz and 1 keV lightcurves to constrain the microphysical parameters associated with the standard afterglow model. The best match between observations and our calculations from the FIREFLY code had fixed parameters of $\epsilon_e = 0.4$, and $\epsilon_B = 0.001$. L. Resmi et al. (2018) and Y. Wu & A. MacFadyen (2018) report $\epsilon_e \sim 0.2$ and 0.3, respectively. Further typical values for ϵ_B lie within the range $\sim 10^{-5}$–10^{-1} (Y. Wu & A. MacFadyen 2018, and references therein). Thus, we find both afterglow parameters agree closely with previous attempts at modeling this afterglow. However, the inherent degeneracy of $E_{\rm iso}/n_{\rm ISM}$ remains, owing to the Blandford–McKee solution of a blast wave. To break this degeneracy, we fix our isotropic equivalent energy closer to the realistic scales of such BNS mergers. We fix $E_{\rm iso} \approx 1.98 \times 10^{51}$ erg, with total jet energy $E_{\rm tot} = 1.6 \times 10^{49}$ erg. This constraints the circumburst medium density $n_{\rm ISM} = 0.1$ cm^{-3}. This value is significantly much larger than 10^{-5}–10^{-3} cm^{-3} suggested by previous studies (D. Lazzati et al. 2018; K. P. Mooley et al. 2018b; R. Margutti et al. 2018), but in agreement with the expected value for such a medium. In contrast, Y. Wu & A. MacFadyen (2018) fix $n_{\rm ISM} = 10^{-3}$ cm^{-3} and obtain $E_{\rm tot} = 2 \times 10^{49}$ erg with a similar model. Table 1 summarizes the parameter values obtained.

Narrowing down all the parameters for the jet–ISM interaction, we then used the sky map feature of FIREFLY by tracking the most luminous region of the GRB 170817A afterglow along the plane perpendicular to the observer. We get an apparent velocity of the afterglow through the sky of $2.12c$ in the initial days, slowing down to $1.6c$ later after the first peak. However, K. P. Mooley et al. (2018a) report the apparent velocity observed as 7 times the speed of light. This contradicts our model and implies a smaller viewing angle. H. Wang et al. (2024) also found a larger viewing angle (∼50°) fit to the afterglow, which reduced to ∼18°.16 after correcting for superluminal motion. Other attempts at modeling the rebrightening with $\theta_{\rm obs} \sim 27°$, include a power-law momentum distribution in the kilonova (A. Kathirgamaraju et al. 2017), a fast moving tail in the dynamical ejecta, and central engine powered radiation from the compact object (see A. Hajela et al. 2019, and references therein for a detailed discussion).

We conclude that it is possible to associate a rebrightening time with the counterjet visibility time and constrain the observer angle from that. For GRB 170817A/GW170817 we can further fine-tune the model to match the radio and X-ray lightcurves for that observer angle. However, although the association of counterjet visibility with excess flux timescale and lightcurve matching indicates a possible solution to the X-ray excess, this does explain the radio band observations. Only by comparing the apparent motion of the object through the sky, we can nullify this seeming correlation. Hence we propose that the jet and counterjet rebrightening timescales can also be used to constrain the observer's orientation with respect to the jet. Further, full diagnostics including the apparent (superluminal) motion along with parameter estimation with lightcurve fitting is required to narrow down the geometrical orientation for such beamed emissions observed off axis.

Acknowledgments

We acknowledge D. Giannios, H. Wang, G. Ryan, and H. van Eerten for their helpful comments, and H. van Eerten for also helping set up Boxfit. We also acknowledge A. Hajela for discussions on the new data from GW170817A. Hydrodynamical calculations were carried out on the Petunia cluster at Purdue University. This project and the development of the code FIREFLY was supported by NASA under grant No. 80NSSC22K1615.

ORCID iDs

Ranadeep G. Dastidar https://orcid.org/0009-0000-6548-6177
Paul C. Duffell https://orcid.org/0000-0001-7626-9629

References

Bell, A. R. 1978, MNRAS, 182, 147
Blandford, R. D., & McKee, C. F. 1976, PhFl, 19, 1130
Blandford, R. D., & Ostriker, J. P. 1978, ApJL, 221, L29
Cantiello, M., Jensen, J. B., Blakeslee, J. P., et al. 2018, ApJL, 854, L31
Coulter, D. A., Foley, R. J., Kilpatrick, C. D., et al. 2017, Sci, 358, 1556
Duffell, P. C., & MacFadyen, A. I. 2013, ApJL, 776, L9
Duffell, P. C., Quataert, E., Kasen, D., & Klion, H. 2018, ApJ, 866, 3
Fong, W., Blanchard, P. K., Alexander, K. D., et al. 2019, ApJL, 883, L1
Ghirlanda, G., Salafia, O. S., Paragi, Z., et al. 2019, Sci, 363, 968
Granot, J., & Loeb, A. 2003, ApJ, 593, L81
Granot, J., & Sari, R. 2002, ApJ, 568, 820
Hajela, A., Margutti, R., Alexander, K. D., et al. 2019, ApJL, 886, L17
Hajela, A., Margutti, R., Bright, J. S., et al. 2022, ApJL, 927, L17
Hotokezaka, K., Kiuchi, K., Shibata, M., Nakar, E., & Piran, T. 2018, ApJ, 867, 95
Hotokezaka, K., Nakar, E., Gottlieb, O., et al. 2019, NatAs, 3, 940
Kathirgamaraju, A., Barniol Duran, R., & Giannios, D. 2017, MNRAS: Letters, 473, L121
Kathirgamaraju, A., Tchekhovskoy, A., Giannios, D., & Barniol Duran, R. 2019, MNRAS: Letters, 484, L98
Lazzati, D., Perna, R., Morsony, B. J., et al. 2018, PhRvL, 120, 241103
Li, L.-B., Geng, J.-J., Huang, Y.-F., & Li, B. 2019, ApJ, 880, 39
Li, Z., & Song, L. M. 2004, ApJ, 614, L17
Margutti, R., Alexander, K. D., Xie, X., et al. 2018, ApJL, 856, L18
Metzger, B. D. 2017, arXiv:1710.05931
Mooley, K. P., Deller, A. T., Gottlieb, O., et al. 2018a, Natur, 561, 355
Mooley, K. P., Nakar, E., Hotokezaka, K., et al. 2018b, Natur, 554, 207
Nakar, E., & Piran, T. 2018, MNRAS, 478, 407
Nathanail, A., Gill, R., Porth, O., Fromm, C. M., & Rezzolla, L. 2021, MNRAS, 502, 1843
Piran, T. 2005, RvMP, 76, 1143
Resmi, L., Schulze, S., Ishwara-Chandra, C. H., et al. 2018, ApJ, 867, 57
Ryan, G., van Eerten, H., Troja, E., et al. 2024, ApJ, 975, 131
Salafia, O. S., Ghisellini, G., & Ghirlanda, G. 2017, MNRAS: Letters, 474, L7
Sari, R., Piran, T., & Halpern, J. 1999, ApJ, 519, L17
Sari, R., Piran, T., & Narayan, R. 1998, ApJ, 497, L17
Troja, E., O'Connor, B., Ryan, G., et al. 2021, MNRAS, 510, 1902
Troja, E., Piro, L., Ryan, G., et al. 2018, MNRAS: Letters, 478, L18
Troja, E., Piro, L., van Eerten, H., et al. 2017, Natur, 551, 71
Troja, E., van Eerten, H., Zhang, B., et al. 2020, MNRAS, 498, 5643
van Eerten, H. 2013, arXiv:1309.3869
van Eerten, H., Zhang, W., & MacFadyen, A. 2010, ApJ, 722, 235
Wang, H., Dastidar, R. G., Giannios, D., & Duffell, P. C. 2024, ApJS, 273, 17
Wang, X., Huang, Y., & Kong, S.-W. 2009, A&A, 505, 1213
Wu, Y., & MacFadyen, A. 2018, ApJ, 869, 55
Zhang, F.-W., Fan, Y.-Z., Shao, L., & Wei, D.-M. 2013, ApJL, 778, L11
Zhang, W., & MacFadyen, A. 2009, ApJ, 698, 1261